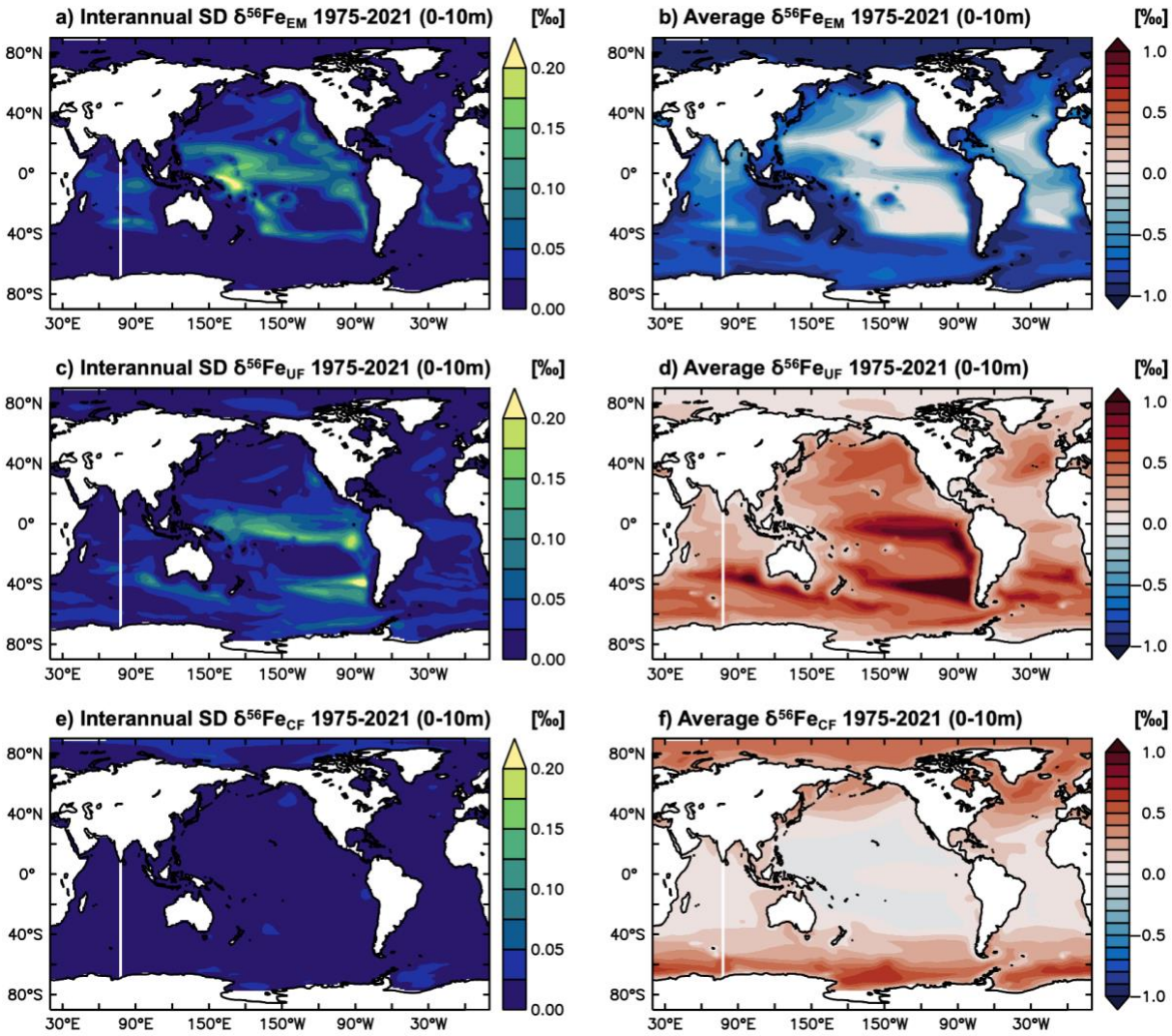

Figure S1. Surface ocean interannual variability of $\delta^{56}Fe_{diss}$ drivers in the present climate (1975-2021). Surface ocean (0-10m) interannual SD and average values of (a,b) $\delta^{56}Fe_{EM}$, (c,d) $\delta^{56}Fe_{UF}$, and (e,f) $\delta^{56}Fe_{CF}$ from the hindcast experiment.

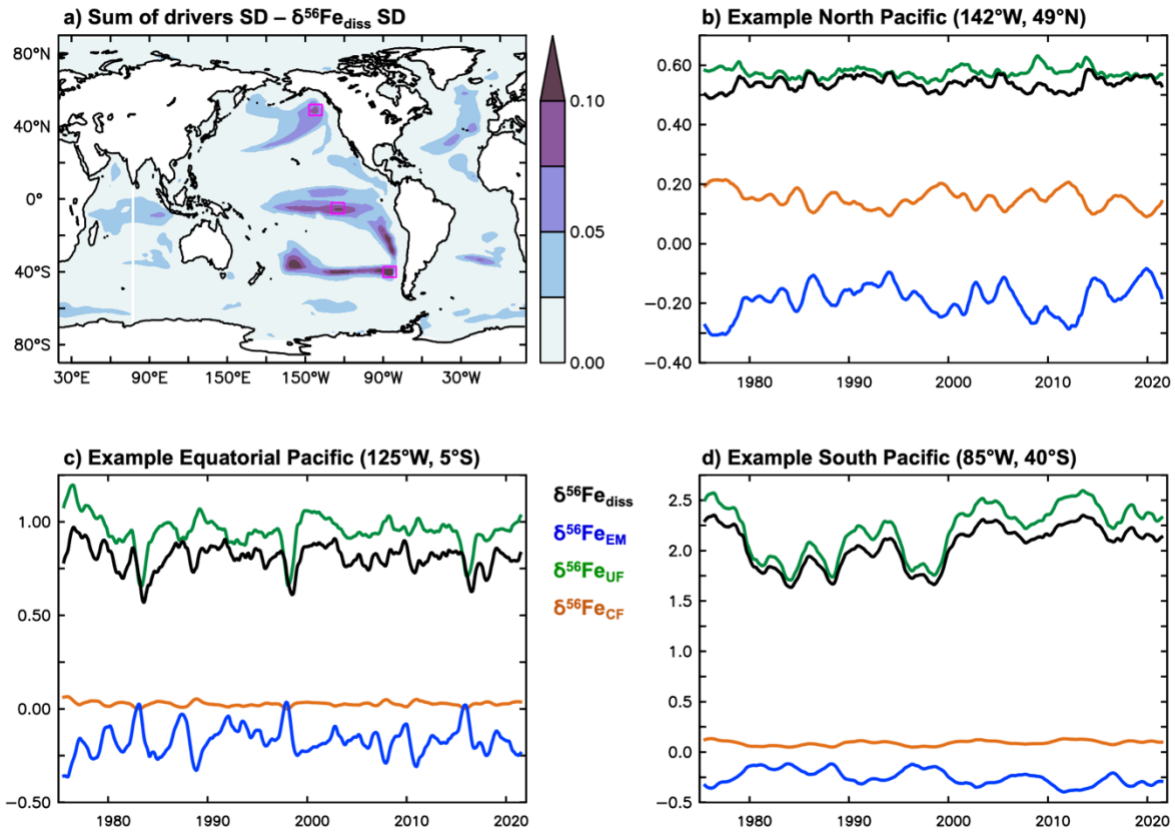

Figure S2. Opposing effects of $\delta^{56}Fe_{diss}$ variability drivers in the present climate. (a) Difference between the sum of SDs of the three drivers and the overall $\delta^{56}Fe_{diss}$ (i.e., SD $\delta^{56}Fe_{UF}$ + SD $\delta^{56}Fe_{CF}$ + SD $\delta^{56}Fe_{EM}$ - SD $\delta^{56}Fe_{diss}$), indicating areas where temporal changes in different drivers (partially) cancel each other out. (b-d) Time series of $\delta^{56}Fe_{diss}$, $\delta^{56}Fe_{EM}$, $\delta^{56}Fe_{UF}$ and $\delta^{56}Fe_{CF}$ at three exemplary locations in the north, equatorial, and south Pacific, which illustrate how two (or more) drivers can have opposing effects in time, leading to decreased overall $\delta^{56}Fe_{diss}$ variability. In the North Pacific (b), variability of the two dominant drivers $\delta^{56}Fe_{EM}$ and $\delta^{56}Fe_{CF}$ is opposite, as in times with high external input of light $\delta^{56}Fe_{diss}$ (i.e., more negative $\delta^{56}Fe_{EM}$ effect), stronger complexation fractionation effects lead to heavier $\delta^{56}Fe_{diss}$ (i.e., more positive $\delta^{56}Fe_{CF}$ effect). This opposing behaviour leads to very little residual $\delta^{56}Fe_{diss}$ variability. In the two other examples in the Equatorial (c) and South Pacific (d), the opposing drivers are $\delta^{56}Fe_{UF}$ and $\delta^{56}Fe_{EM}$. However, $\delta^{56}Fe_{diss}$ variability is still substantial in both cases since the effects are either not perfectly opposite (equatorial Pacific; c) or the effect of the opposing driver ($\delta^{56}Fe_{EM}$) is weaker than for the dominant driver ($\delta^{56}Fe_{UF}$; south Pacific; d).

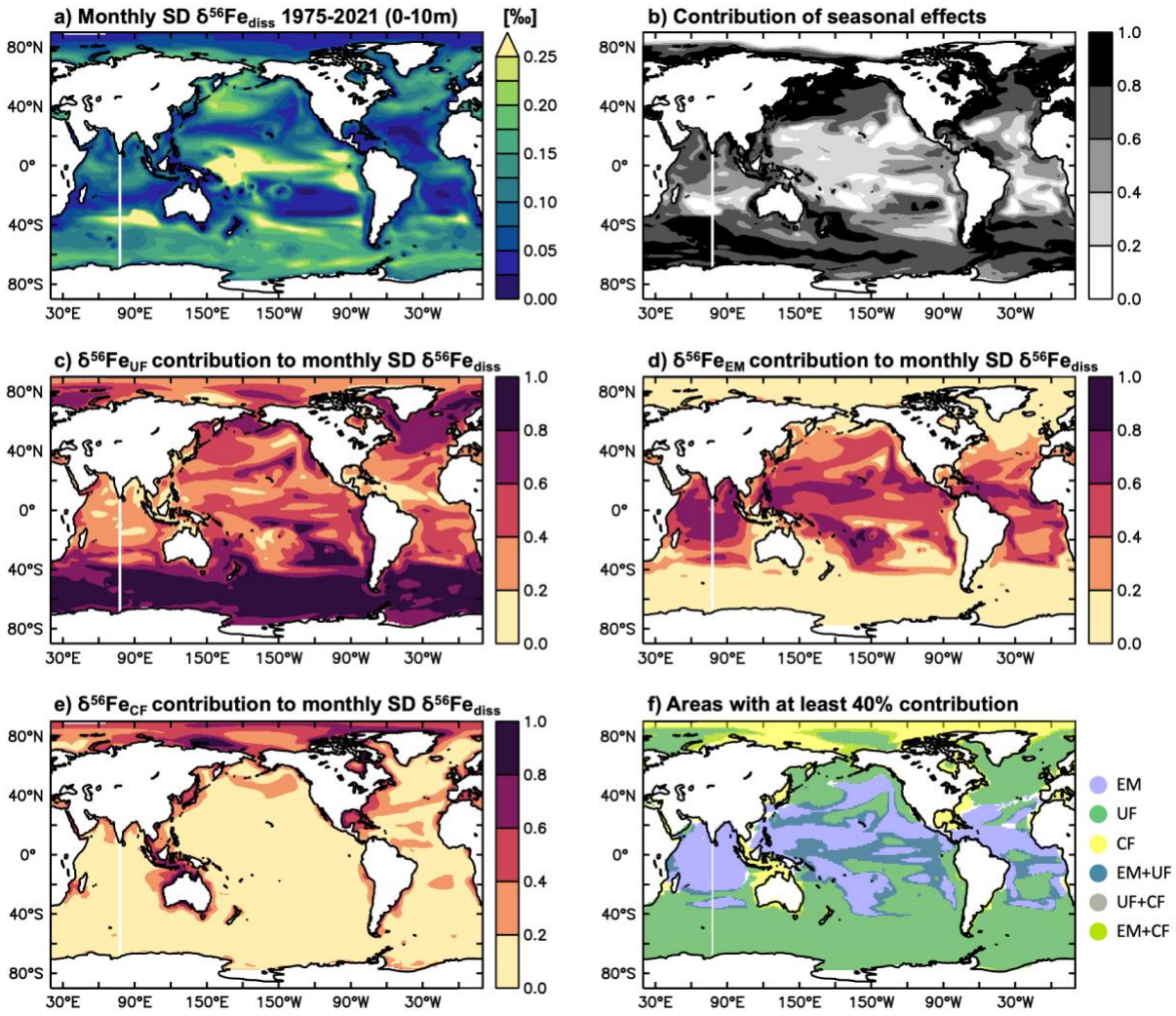

Figure S3: Surface ocean $\delta^{56}Fe_{diss}$ seasonal and interannual variability in the present climate (1975-2021). (a) Surface ocean (0-10m) monthly $\delta^{56}Fe_{diss}$ SD, calculated from monthly hindcast experiment outputs without applying a 12-month running mean. (b) Contribution of seasonal effects to the monthly $\delta^{56}Fe_{diss}$ SD, calculated as follows: $\frac{monthly\ SD\ \delta^{56}Fe_{diss} - interannual\ SD\ \delta^{56}Fe_{diss}}{monthly\ SD\ \delta^{56}Fe_{diss}}$. Respective contributions of (c) $\delta^{56}Fe_{UF}$, (d) $\delta^{56}Fe_{EM}$, and (e) $\delta^{56}Fe_{CF}$ to the monthly $\delta^{56}Fe_{diss}$ variability, and (f) a map of which driver(s) is locally dominant (i.e., contributing over 40% of the sum of the monthly $\delta^{56}Fe_{diss}$ SD).

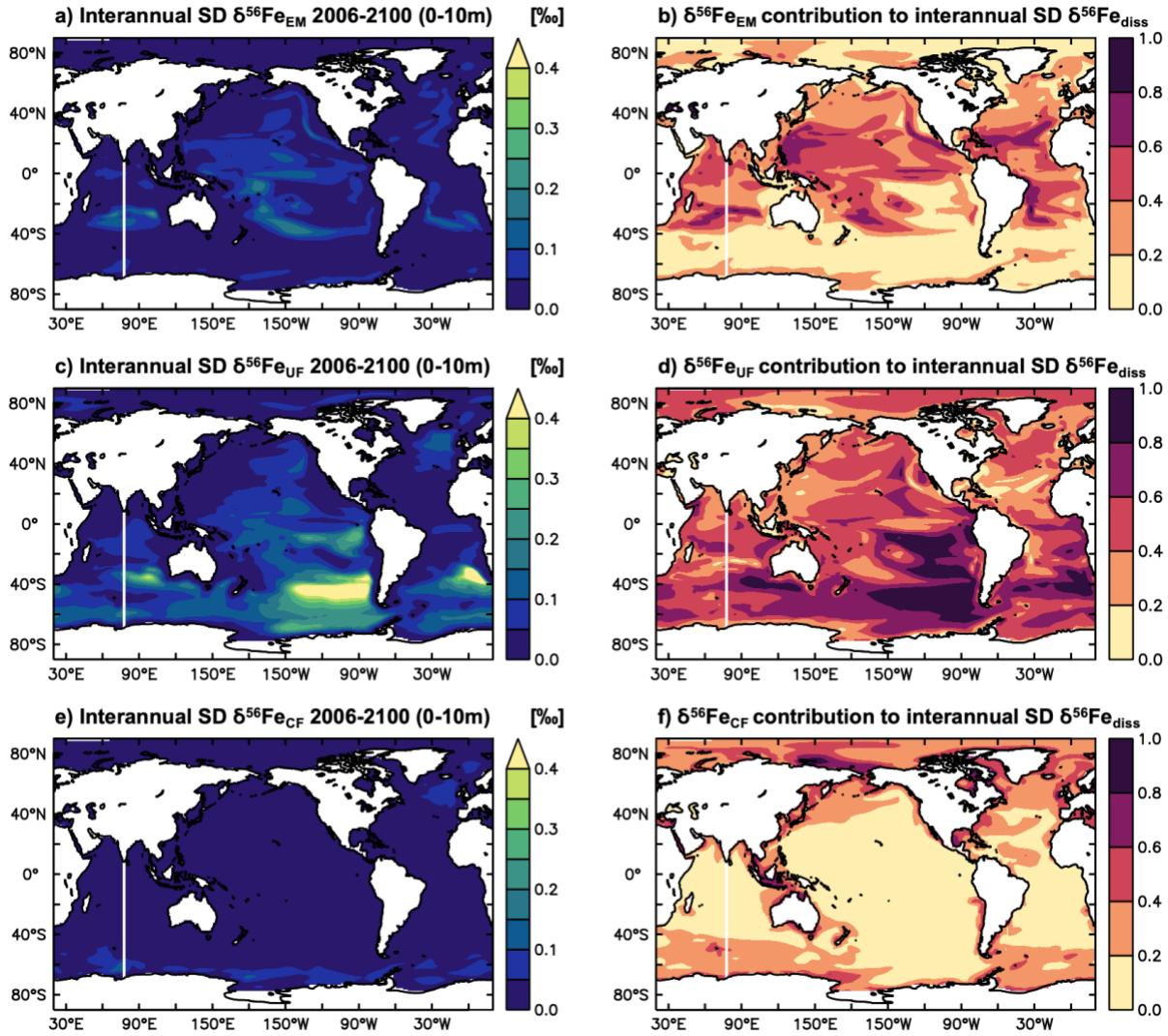

Figure S4. Surface ocean variability of $\delta^{56}Fe_{diss}$ drivers under climate change conditions (2006-2100). Surface ocean (0-10m) interannual SD and contribution to $\delta^{56}Fe_{diss}$ variability of (a,b) $\delta^{56}Fe_{EM}$, (c,d) $\delta^{56}Fe_{UF}$, and (e,f) $\delta^{56}Fe_{CF}$, calculated for climate change experiments.

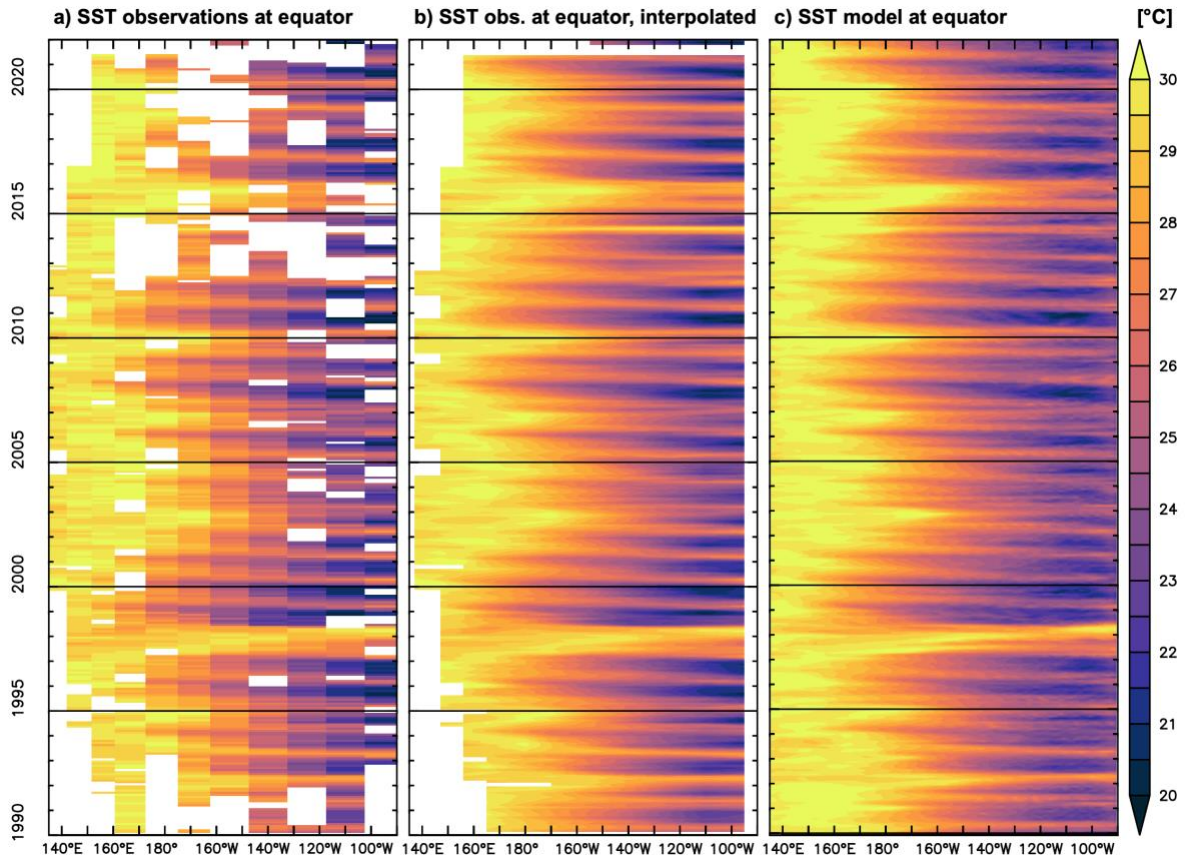

Figure S5: Comparison of hindcast model simulations to observations in the tropical Pacific. (a) Original and (b) interpolated observations of SST at the equator, and (c) the corresponding model output. Monthly-average SST observations were obtained from the TAO/TRITON moored buoy array (TAO Project Office of NOAA/PMEL) for the period of January 1979 to December 2021. A statistical comparison of the hindcast model output to the entire TAO/TRITON SST data (i.e., including data north/south of the equator) shows excellent agreement (R: 0.98, RMSE: 0.46°C).

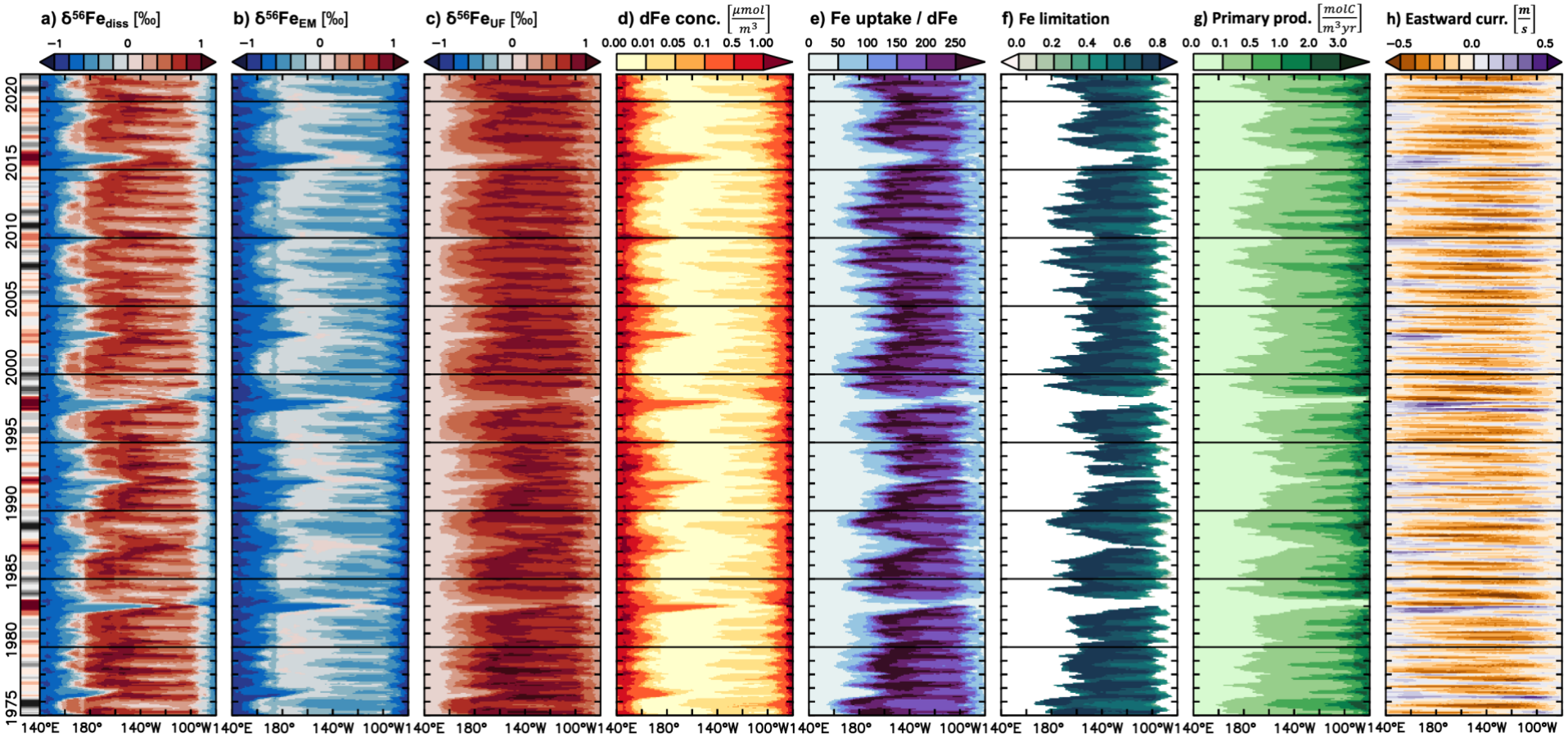

Figure S6: Mechanisms behind surface ocean $\delta^{56}Fe_{diss}$ changes in the equatorial Pacific. Time series (1975-2021) of monthly-mean surface ocean (a) $\delta^{56}Fe_{diss}$, (b) $\delta^{56}Fe_{EM}$, (c) $\delta^{56}Fe_{UF}$, (d) dFe concentration, (e) ratio between Fe uptake and dFe concentration, (f) Fe limitation, (g) primary production, and (d) upper ocean (0-50m average) eastward currents of the hindcast experiments, averaged from 5°N to 5°S. The Ocean Nino Index is included on the left side (red: El Niño, Grey: La Niña).

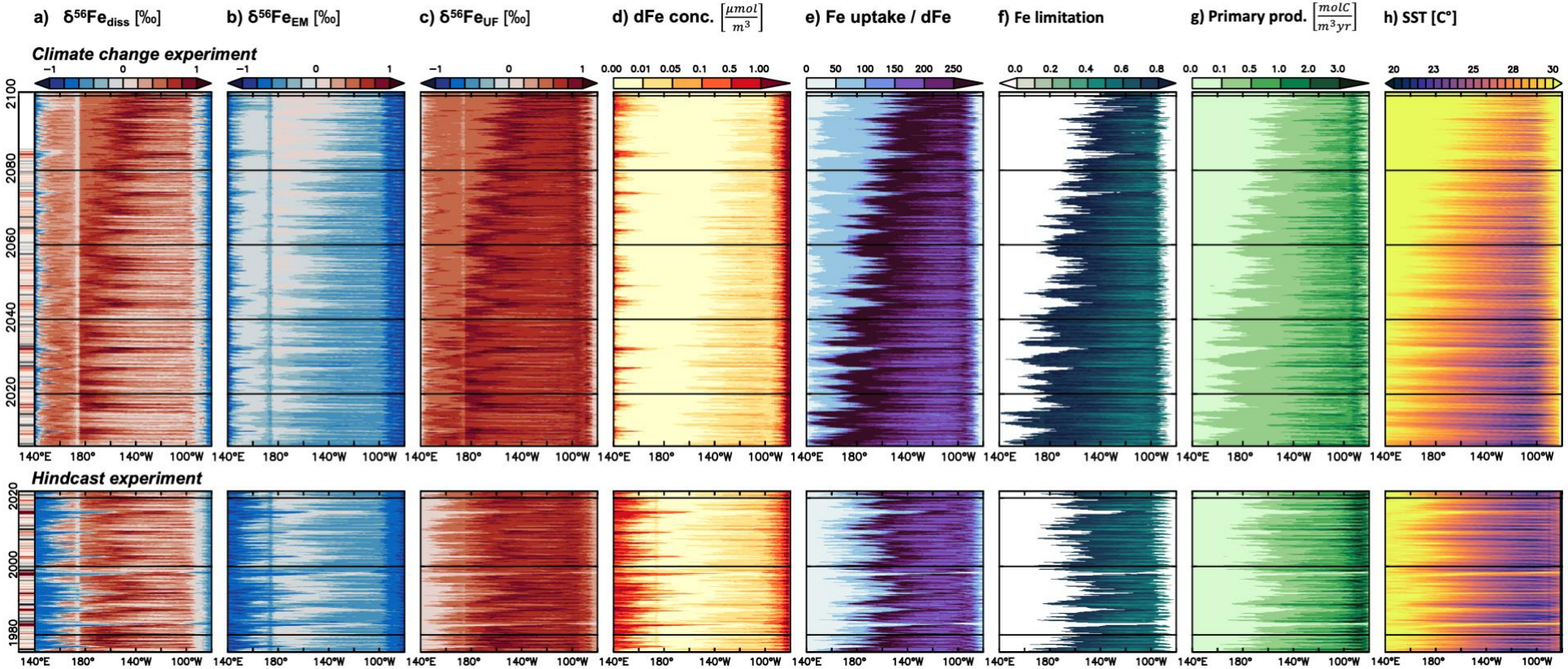

Figure S7: Mechanisms behind climate-change related surface ocean $\delta^{56}Fe_{diss}$ variability in the equatorial Pacific (at 0°). Upper section: Time series (2006-2100) of monthly-mean surface ocean (a) $\delta^{56}Fe_{diss}$, (b) $\delta^{56}Fe_{EM}$, (c) $\delta^{56}Fe_{UF}$, (d) dFe concentration, (e) ratio between Fe uptake and dFe concentration, (f) Fe limitation, (g) primary production, and (h) temperature of the climate change experiments. Lower section: Same parameters taken from the hindcast experiments. The Ocean Nino Index is included on the left side (red: El Niño, Grey: La Niña), whereby for the climate change experiment, the SST anomalies in the ENSO 3.4 region were calculated by subtracting 30 year running mean SST data from the monthly SST. Note that these plots were extracted from the equator (i.e., averaged over 0.5°S to 0.5°N instead of ±5°), as climate change induced $\delta^{56}Fe_{diss}$ changes are most pronounced here (Figure 2). Discrepancies between climate change and hindcast experiments, such as $\delta^{56}Fe_{diss}$ variability in the west, are due to differences in circulation patterns, which are most likely more realistic for the hindcast experiment, as it was forced by an atmospheric reanalysis product (see Figure S5)

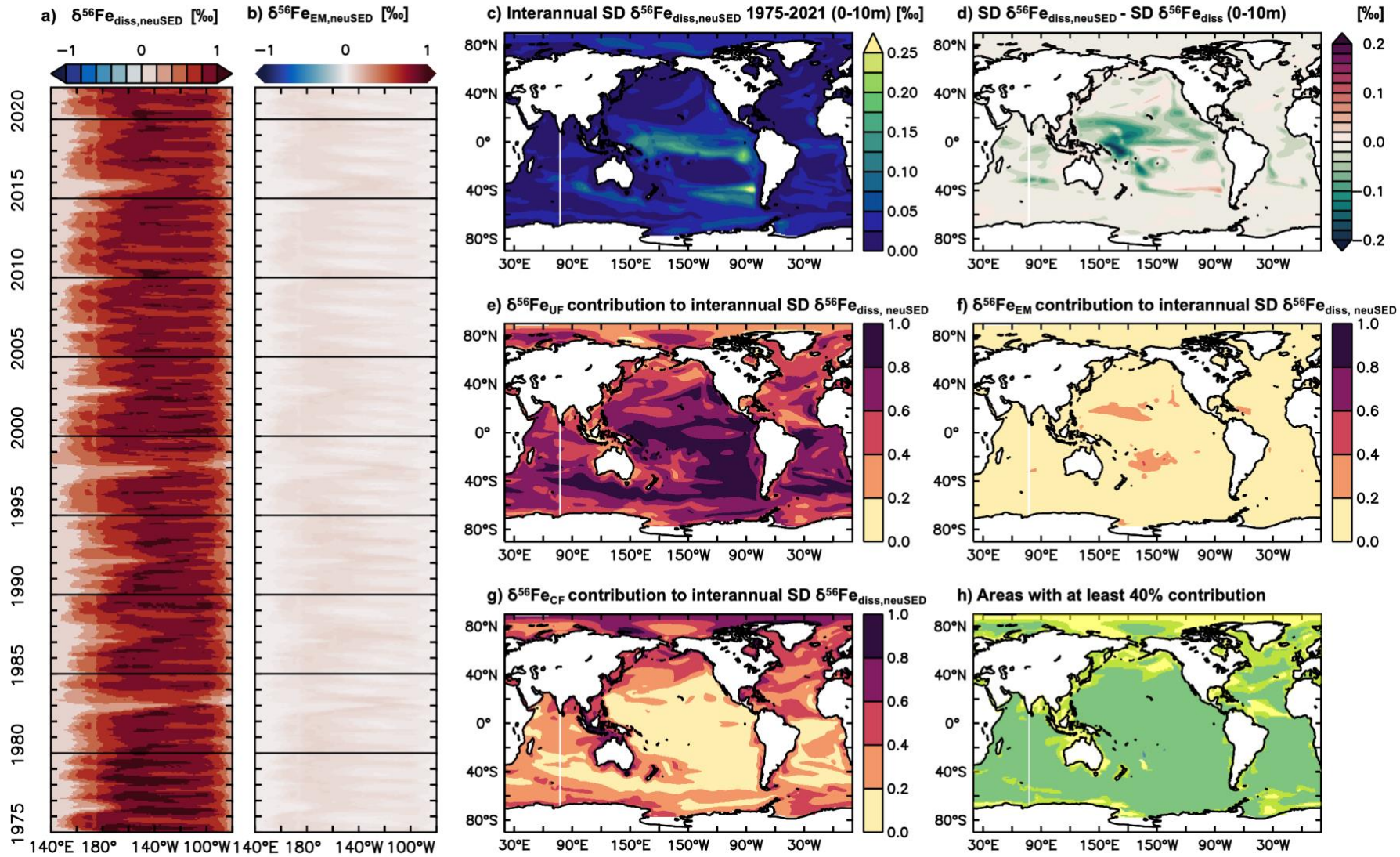

Figure S8: Impact of light sediment Fe on $\delta^{56}Fe_{diss}$ variability. Time series of surface ocean (a) $\delta^{56}Fe_{diss}$ and (b) $\delta^{56}Fe_{EM}$ in the tropical Pacific (5°S to 5°N average) for a hindcast experiment with neutral (0‰) sediment endmember (denoted a "SN"); (c) interannual SD $\delta^{56}Fe_{diss}$ of the same experiment, (d) difference between SD $\delta^{56}Fe_{diss,SN}$ and SD $\delta^{56}Fe_{diss}$ of the hindcast standard, contribution of (e) $\delta^{56}Fe_{UF,SN}$, (f) $\delta^{56}Fe_{EM,SN}$, and (g) $\delta^{56}Fe_{CF,SN}$ to SD $\delta^{56}Fe_{diss,SN}$ and (h) a map of which driver(s) is locally dominant (i.e., contributing over 40% of the sum of SD).

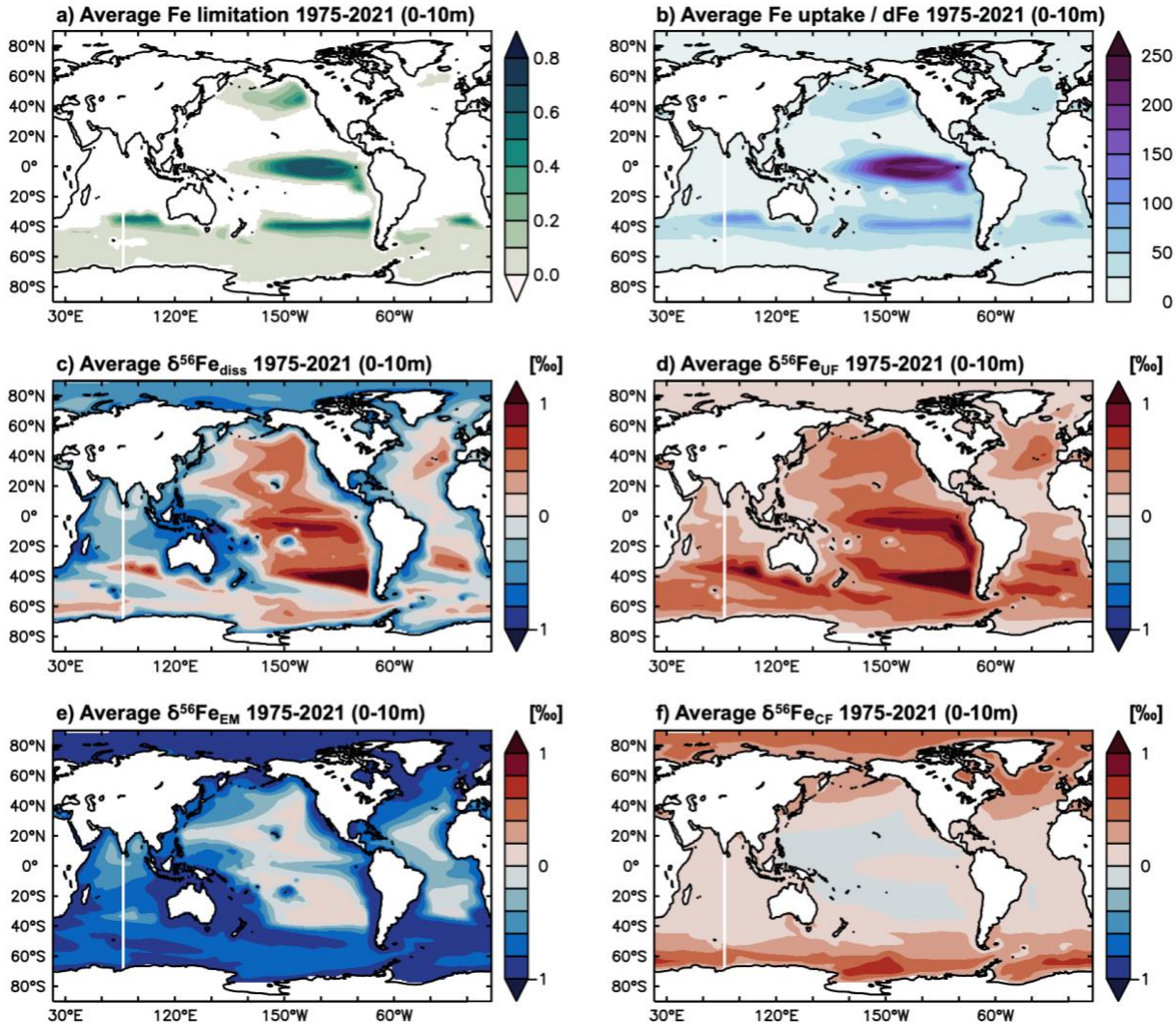

Figure S9. Connection between surface ocean Fe limitation and $\delta^{56}Fe_{diss}$ in the present climate (1975-2021). Surface ocean (0-10m) average values of (a) Fe limitation, (b) Fe uptake to dFe concentration ratio, (c) $\delta^{56}Fe_{diss}$, (d) $\delta^{56}Fe_{UF}$, (e) $\delta^{56}Fe_{EM}$ and (f) $\delta^{56}Fe_{CF}$ of the hindcast experiments. Note that Fe is usually limiting phytoplankton growth where the ratio between Fe uptake rates and dFe concentration is high, with some exceptions (e.g., in the North Atlantic). Meanwhile, a high Fe uptake to dFe concentration ratio generally leads to heavy $\delta^{56}Fe_{UF}$, although in some areas such as the south Pacific, $\delta^{56}Fe_{UF}$ is heavier than would be expected from this ratio.